# Microstructure, ferromagnetic resonance, and electrical analysis of Ho-substituted Li-Ni nanoparticles

Alina Manzoor [a,*], Aamir Shahzad [a], Wolfgang Kuch [b], Tauqir Shinwari [b], Ivar Kumberg [b], Yasser A. Shokr [b,c], Muhammad Azhar Khan [d,*]

[a] Department of Physics, Government College University, Faisalabad 38000, Pakistan
[b] Institut für Experimentalphysik, Freie Universität Berlin, Arnimallee 14, Berlin 14195, Germany
[c] Faculty of Science, Department of Physics, Helwan University, Cairo 17119, Egypt
[d] Institute of Physics, The Islamia University of Bahawalpur, Bahawalpur 63100, Pakistan

## ABSTRACT

The substitution of rare earth ions is a novel approach to vary the dynamic magnetic properties of soft ferrites to such an extent that its electrical properties and ferromagnetic resonance (FMR) response can be set over a broad frequency range. In this work, a complete transmission electron microscopy (TEM), scanning electron microscopy (SEM), ferromagnetic resonance spectroscopy (FMR), X-ray photoelectron spectroscopy (XPS), and current-voltage (I-V) analysis of holmium (Ho) substituted lithium-nickel soft ferrites with composition $Li_{1.2}Ni_{0.4}Fe_{2-x}Ho_xO_4$ (x = 0, 0.03, 0.06, 0.09, 0.12, and 0.15) is carried out. TEM analysis reveals a spherical shape distribution of nanoparticles with a particle size of $\sim$ 50 nm. FMR study is carried out to check the role of Ho addition on magnetic energy losses, FMR line position, and shape. The shift in FMR line shape is mainly attributed to the anisotropy contribution, relaxation processes, and ferromagnetic interactions between the magnetic nanoparticles. XPS experiments confirm the presence of all compositional elements along their valence states. The Ho substitution increased the electrical resistivity, whereas the damping of A-B exchange interactions resulted in a decline of Curie temperature ($T_c$), which is required for high-frequency power applications.

## 1. Introduction

One of the main objectives of developing new nanomagnetic materials is energy saving. Among a variety of investigated nanomaterials, soft ferrites with spinel structure appear as representative materials for the modern industry as they offer high resistivity connected with significantly low eddy current losses, low core losses, relatively low coercivity, high magnetization, low magnetic losses, and a high data storage efficiency [1]. Ferrites being a prominent class of magnetic oxide materials, are in high demand as a material option for high-frequency inductive cores and inductors due to their size, weight, high resistivity, low energy losses, compact core shape, and inexpensive fabrication as the miniaturization of inductive components in power electronic devices and increasing operational frequencies is prerequisite for various electronic industry applications. Soft ferrites are widely used for energy transfer in converters and switch-mode power supplies. Minimizing the magnetic energy losses (microwave losses) is the key goal of the study on advanced ferrites; however, to obtain high

efficiency, detailed knowledge and interpretation of the dissipative processes over a wide range of frequencies are needed [2].

The origin of damping or microwave losses in ferrites is commonly attributed to relaxation mechanisms such as valence exchange, two-magnon scattering, eddy current dissipation, domain wall rotation, and relaxing impurities [3–7]. In a frequency-dependent mode, domain-wall-motion and rotational processes contribute to the magnetization reversal and deliver energy to the crystal lattice by a motion deterioration of the precessing spins or conduction charges (eddy currents) [8]. In addition, a dense crystal structure may also reduce magnetic energy losses. So, this study's main objective is to produce ultra-dense polycrystalline ferrites with low porosity, high electrical resistivity, and reduced magnetic energy losses.

Li-Ni based ferrites offer their role in various device applications such as microwave and telecommunication devices [9]. However, their performance can be enhanced by incorporating rare-earth (RE) elements into the spinel lattice of this system [10]. Many researchers have investigated the role of RE elements on the electromagnetic properties of
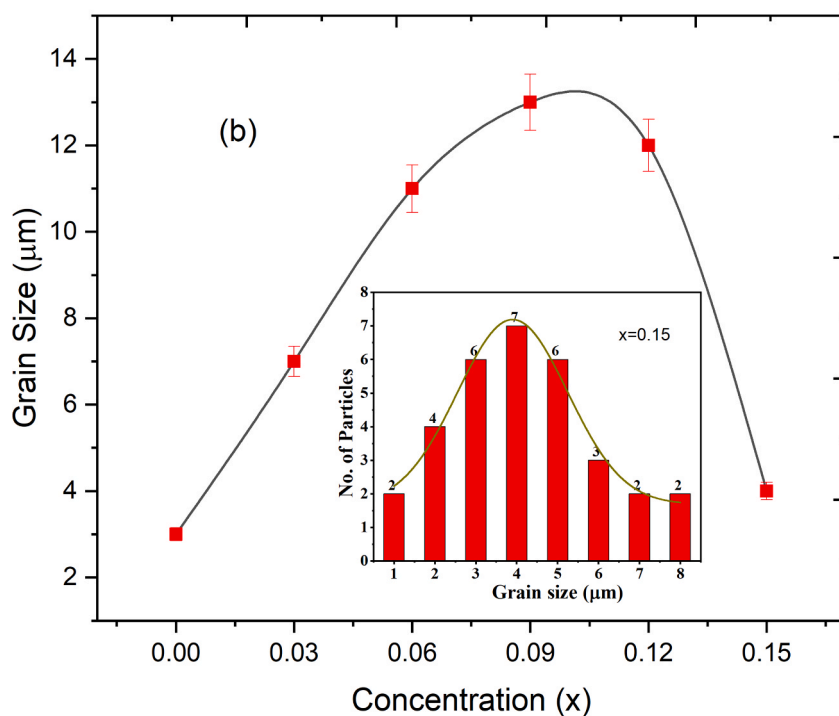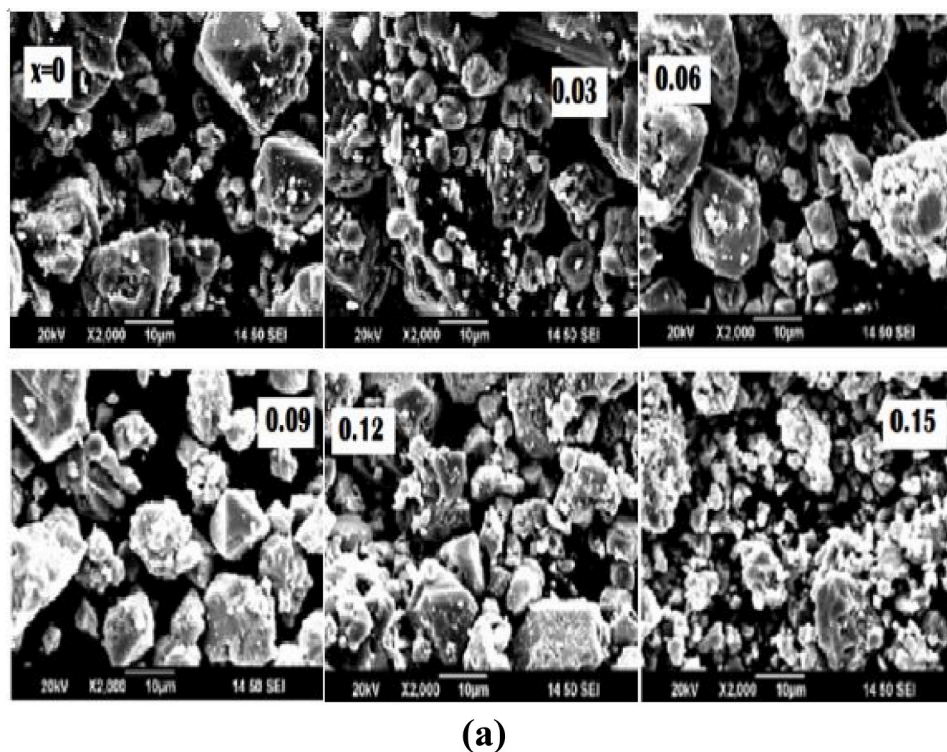
---

\* Corresponding authors.

*E-mail addresses:* alinamanzoor@hotmail.com (A. Manzoor), azhar.khan@iub.edu.pk (M.A. Khan).

**(a)**



**Fig. 1.** a) SEM images of $Li_{1.2}Ni_{0.4}Ho_xFe_{2-x}O_4$ ($0.0 \leq x \leq 0.15$) ferrite powders. b) Grain size vs. Ho concentration obtained from SEM images of $Li_{1.2}Ni_{0.4}$-$Ho_xFe_{2-x}O_4$ ($0.0 \leq x \leq 0.15$) ferrite powders. The inset of Figure (b) depicts the size histogram for the composition x = 0.15.

Li-Ni ferrites, which are significantly improved as compared to those of unsubstituted Li-Ni ferrites [9–12].

Besides the formulation and processing, selecting appropriate additives for the spinel structure of soft ferrites plays a crucial role in influencing the performance of Li-Ni ferrites [13]. In this study, holmium is substituted in the Li-Ni ferrite system not only because of its large intrinsic magnetic moment (10.6 $\mu_B$) and strong anisotropy field, but also due to its highly resistive nature, which can consequently reduce the ferromagnetic losses and enhance the electrical resistivity. Such optimized electromagnetic properties will support this system for use in high-frequency applications such as microwave devices. The substitution of $Ho^{3+}$ for $Fe^{3+}$ in Li-Ni ferrites increases the resistivity (less energy dissipation) and leads to low microwave losses beneficial to tailor the electromagnetic behavior of these materials, which is desired for inductive cores and microwave applications [14]. The FMR line width and resonance position also depend on cation ordering. To the best of our literature survey, the effect of Ho ions on the FMR losses and electrical properties of Li-Ni based ferrites has not been explored yet.
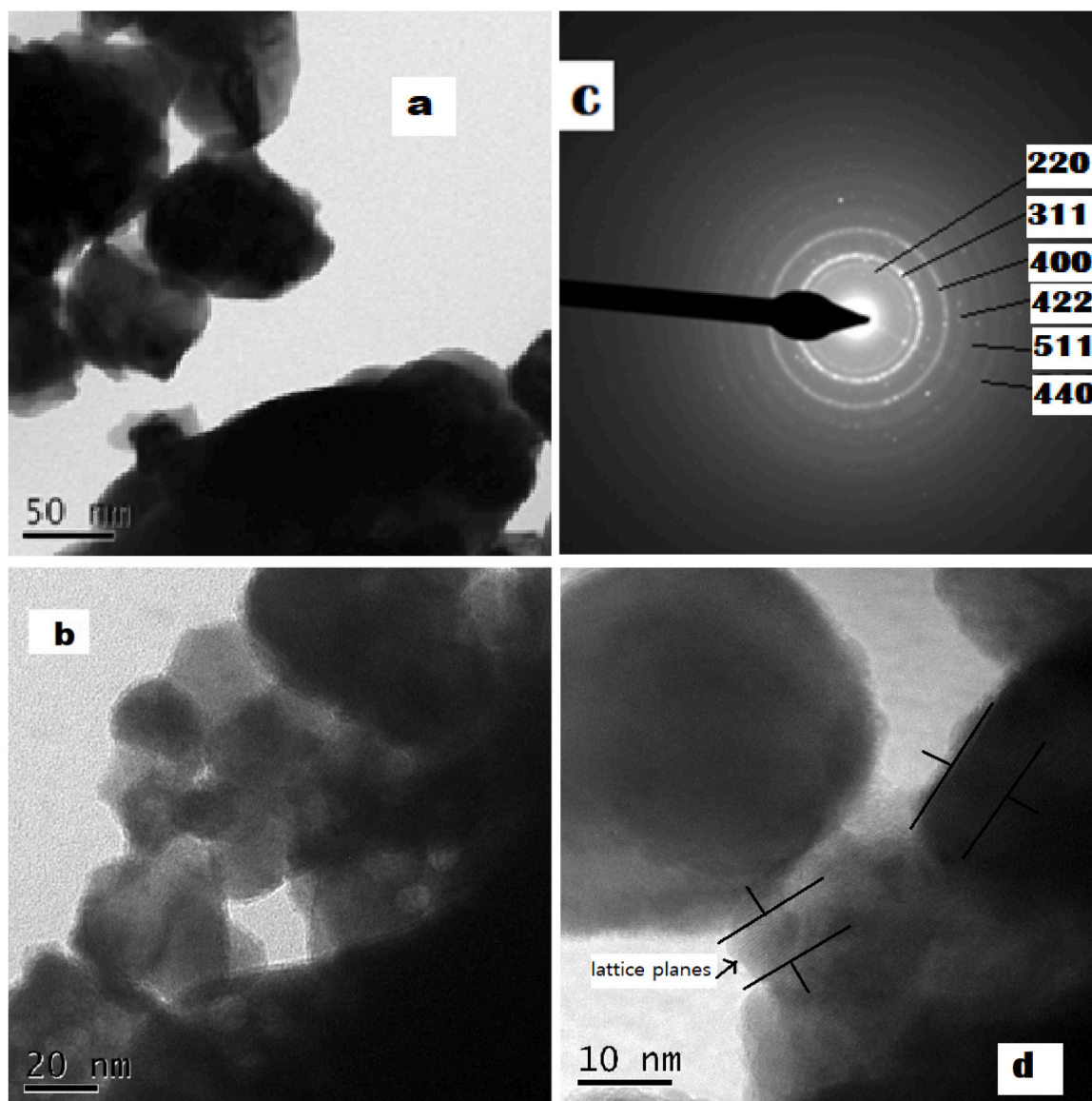
**Fig. 2.** (a, b) TEM images of $Li_{1.2}Ni_{0.4}Ho_{0.09}Fe_{1.91}O_4$ at 50 nm and 20 nm scale (c) SAED image and (d) HRTEM view of $Li_{1.2}Ni_{0.4}Ho_{0.09}Fe_{1.91}O_4$ ferrite. Atomic lattice planes are recognized in the areas marked by black lines.

Furthermore, the literature needs a detailed understanding of the temperature-dependent electrical properties and contribution of FMR linewidth in Ho-substituted Li-Ni polycrystalline ferrites. So, here we focus on investigating the role of holmium incorporation on various magnetic and electric characteristics of lithium-based nano polycrystalline ferrites, i.e., $Li_{1.2}Ni_{0.4}Ho_xFe_{2-x}O_4$ (x = 0, 0.03, 0.06, 0.09, 0.12, and 0.15). The 15% is the maximum Ho concentration at which Ho is settled in the lattice matrix, after that it starts to segregate at the grain boundaries [15].

## 2. Experimental

The synthesis, structural, dielectric, spectral, and magnetic analysis of $Li_{1.2}Ni_{0.4}Ho_xFe_{2-x}O_4$ (x = 0, 0.03, 0.06, 0.09, 0.12, and 0.15) soft ferrites fabricated via the sol-gel auto combustion method is reported in the previous part of this study [15]. The Ho-substituted soft ferrites with composition $Li_{1.2}Ni_{0.4}Ho_xFe_{2-x}O_4$ (x = 0, 0.03, 0.06, 0.09, 0.12, and 0.15) are synthesized via sol-gel method. The prepared samples are sintered at 950 °C for 6 hr in a box furnace under air environment for the removal of organic residuals and the development of face-centered cubic

structure. The details of the synthesis process are reported in the previous part [15]. In this part, a detailed analysis by SEM, XPS, TEM, FMR, and I-V is presented. Room-temperature FMR analysis was done through an E-LINE century series EPR spectrometer, operating in the X-band (~8.9 GHz). The sintered powders were pressed into circular pellets to investigate the electrical properties (I-V) by employing a two-probe technique through a Keithley LCR meter model-197. The experimental setup for XPS consists of a home-made ultra-high vacuum (UHV) chamber with a non-monochromatized X-ray source (VG), a 100 mm hemispherical electron energy analyzer with 2D channel plate detection (Specs), and a sample holder where tested materials can be loaded. The spectra presented here are acquired at room temperature with Mg $K_\alpha$ radiation and an analyzer pass energy of 20 eV. TEM Philips CM 12 (LMC) with a 2k x 2k CCD camera and 200 kV accelerating voltage is used for the structural characterizations. An Emcraft SEM microscope (Model. Cube 10) with magnification $3 \times 10^5$ is used for the study of the microstructure.

**Table 1**
Cation distribution of the Ho-doped Li-Ni spinel ferrite samples.

| Samples | Site radii (Å) | | Bond length (Å) | | Shared edges | | Unshared edges |
|---|---|---|---|---|---|---|---|
| | $r_A$ | $r_B$ | $R_A$ | $R_B$ | dAE | dBE | dBEU |
| 0.00 | 0.5405 | 0.6830 | 1.8905 | 2.0342 | 3.0872 | 2.8044 | 2.9475 |
| 0.03 | 0.5411 | 0.6836 | 1.8911 | 2.0349 | 3.0882 | 2.8053 | 2.9484 |
| 0.06 | 0.5407 | 0.6832 | 1.8907 | 2.0344 | 3.0874 | 2.8046 | 2.9477 |
| 0.09 | 0.5403 | 0.6828 | 1.8903 | 2.0340 | 3.0869 | 2.8041 | 2.9472 |
| 0.12 | 0.5394 | 0.6818 | 1.8894 | 2.0331 | 3.0854 | 2.8028 | 2.9458 |
| 0.15 | 0.5391 | 0.6815 | 1.8891 | 2.0327 | 3.0849 | 2.8023 | 2.9453 |

## 3. Results and discussion

### 3.1. SEM study

The surface morphology of the synthesized nanoparticles is investigated by scanning electron microscopy. The SEM micrographs of all the prepared powder samples are shown in Fig. 1a. The aggregation of particles is observed in all samples, which may be attributed to a chemical reaction during the sintering procedure [16]. Relatively weak Van-der-Waals bonds and magnetic forces might be accountable for holding the agglomerated particles together [17]. Moreover, the density of the particles (reduction of pores) increases with increasing Ho concentration, as the micrographs show. The grain histogram is an essential tool used in analyzing SEM images to determine the average grain sizes of distinct ferrite compositions. The size of the grains is measured using ImageJ software and is presented in Fig. 1b. It can be seen from Fig. 1b that the grain size first increases up to x = 0.09 and after that it decreases. The inset of Fig. 1b presents the histogram for the particular composition x = 0.15. Each bin represents a range of sizes, and the height of each bin indicates the number of grains falling within that size range. The resulting histogram visually displays the distribution of particle sizes across the entire sample.

### 3.2. TEM Study

Transmission electron microscopy is a quantitative method to determine nanomaterial particle's size, distribution, and shape. A TEM micrograph of one of the representative samples with composition $Li_{1.2}Ni_{0.4}Ho_{0.09}Fe_{1.91}O_4$ is presented in Fig. 2a. The typical ferrite composition with x = 0.09 shows a particle size of about 50 nm. The particle size of the same sample, as determined from the XRD experiment, is noted to be smaller [15]. The prepared nano-sized ferrite particles are detected to have narrow size spherical distribution and contain multiple nanocrystalline grains (Fig. 2d). Ferrite nanoparticles are also noticed to be slightly agglomerated due to the various kinds of magnetic interactions as well as Van der Waals forces that exist between the ferrite fragments. The SAED view (selected area electron-diffraction) is shown in Fig. 2b, which indicates the formation of bright rings formed by sharp diffraction conditions with well-defined periodicity. Observing the apparent diffraction patterns reveals that the particles are crystallized well. The indexed diffraction rings clarify the high crystallinity of Ho-substituted Li-Ni nano ferrites. High-resolution TEM (HRTEM) provides the direct imaging of the nanoparticles at the atomic scale. The formation of well-developed lattice planes can be confirmed from the HRTEM or phase contrast image, as shown in Fig. 2c.

### 3.3. Cation distribution

The cation distribution of Ho-doped Li-Ni spinel ferrite is estimated using the structural parameters of the prepared samples. The Bertaut method [18] is used to calculate the cation distribution parameters. Cation distributions of the Li, Ni, Ho, and Fe cations at their respective lattice sites (A and B-sites) are estimated from the bond lengths ($R_A$, $R_B$), shared (dAE-dBE), and unshared edges (dBEU), and site radii ($r_A$, $r_B$).
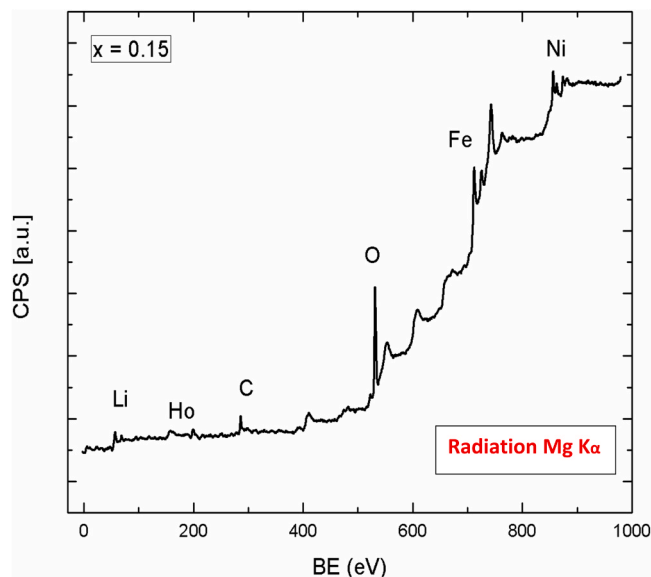
**Fig. 3.** XPS spectrum of $Li_{1.2}Ni_{0.4}Ho_{0.15}Fe_{1.85}O_4$ ferrite sample.

The cation distributions, $R_A$, $R_B$, $r_A$, $r_B$, shared (dAE-dBE), and unshared (dBEU) edges of the Ho-doped Li-Ni nano ferrites are determined using the lattice parameter, and d-spacing. Bertaut's method was used to evaluate these parameters [18]. Table 1 depicts the calculated values of the shared edges, site radii, unshared edges, and bond lengths. The introduction of cations and oxygen ions in the spinel structure is accountable for the alterations of the cation distribution. All cation parameters increase and then decrease with increasing Ho content. This may be because of the variations in the lattice parameter with Ho contents. Similar results have been reported earlier by the researchers [19–21].

### 3.4. XPS analysis

XPS allows to examine the change in chemical (valence) state through a shift in binding energy. The prepared ferrite pellet was mechanically etched before loading into the vacuum chamber for the XPS analysis.

Fig. 3 displays the full-scale XPS spectrum of the $Li_{1.2}Ni_{0.4}Ho_{0.15}$-$Fe_{1.85}O_4$ sample, which confirms the overall composition by identifying the constituents Li, Ni, Fe, Ho, and O. The deconvolution of individual scans for the peaks of all components is shown in Fig. 4. The binding energies of the Fe $2p_{3/2}$ and Fe $2p_{1/2}$ core levels characterize the recorded Fe 2p spectrum. The Fe 2p XPS spectra show that both ferric and ferrous cations co-exist. The $Fe^{2+}$ ions occupy the octahedral sites, while the $Fe^{3+}$ ions reside on both the tetrahedral and octahedral sites. A separation of the peaks at 711.9 and 725.2 eV for Fe $2p_{3/2}$ and Fe $2p_{1/2}$, respectively, into $Fe^{2+}$ and $Fe^{3+}$ ions is not unique and depends on the chosen fit parameters. The Ni $2p_{3/2}$ and Ni $2p_{1/2}$ states correspond to the signals at 856.5 eV and 874.2 eV, respectively. We also see the typical
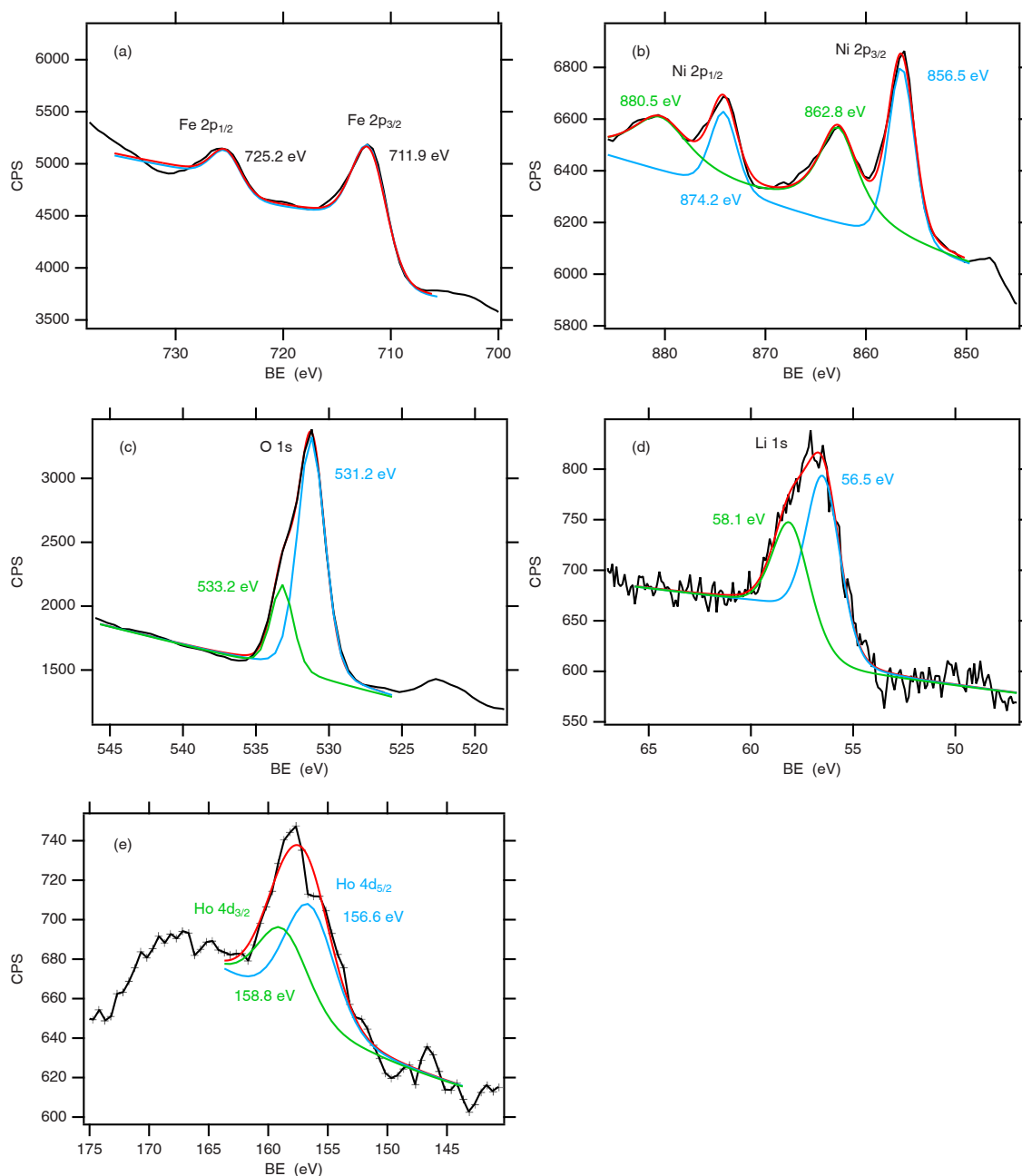
**Fig. 4.** Deconvolution of XPS spectra of a) Fe, b) Ni, c) O, d) Li, and e) Ho of the $Li_{1.2}Ni_{0.4}Ho_{0.15}Fe_{1.85}O_4$ sample.

shake-up satellite peaks at 6.3 eV higher binding energy. The deconvolution of O1s is composed of O1 and O2, which are located at 531.2 and 533.2 eV, respectively. It is generally believed that O1 is the oxygen present in the oxide lattice, whereas O2 is derived from a hydroxyl group adsorbed on the surface [22]. The deconvolution for the Li 1 s metal peak revealed two peaks at 56.5 eV and at 58.1 eV, which may be ascribed to $Li_2CO_3$ and $Li_2O$ [23]. The deconvoluted peaks for Ho 4d at 156.6 eV and 158.8 eV correspond to $Ho^{3+}$ $4d_{5/2}$ and $4d_{3/2}$ states, indicating the incorporation of holmium into the crystal lattice of iron oxide [24]. For charging correction, the readings are corrected concerning the carbon 1 s peak taken at 284.6 eV. Since an unmonochromatized Xray tube was used, satellite peaks due to Mg $K\alpha_{3,4}$ radiation appear at about 9 eV lower binding energy for each peak.

### 3.5. FMR Studies

A single-mode FMR profile is observed at the X-band frequency. The room-temperature ferromagnetic absorption spectra (FMR) for Ho-substituted Li-Ni ferrites are displayed in Fig. 5. The FMR linewidth ($\Delta H$) is examined to reduce from 2056 to 1786 Oe with raising the Ho concentration. The observed decline in $\Delta H$ is well consistent with an increase in bulk density (2.93 – 3.96 g/cm$^3$) or the reduction in porosity (38.5–23.2%), as seen in Fig. 6. The bulk density and porosity calculations have been carried out in the previous part of this research [15]. The bulk density of the pellet is calculated using the relation $\rho_b = m / \pi r^2 h$, where m is the mass of the pellet, r is the radius, and h is the thickness of the pellet sample. The trend of $\Delta H$ is also consistent with the previously reported behavior of $M_s$ (57.9–18.3 emu/g) [15], as listed in Table 2. The variation in the FMR signal is mainly due to the magnetic crystalline anisotropy and ferromagnetic interactions between the magnetic
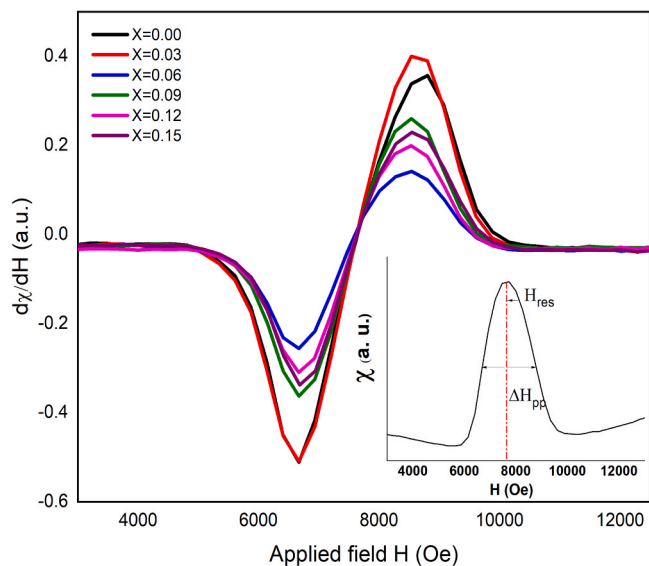
**Fig. 5.** FMR absorption spectra of $Li_{1.2}Ni_{0.4}Ho_xFe_{2-x}O_4$ ferrites. The inset is the integral of the FMR absorption profile of $Li_{1.2}Ni_{0.4}Fe_2O_4$ ferrite.
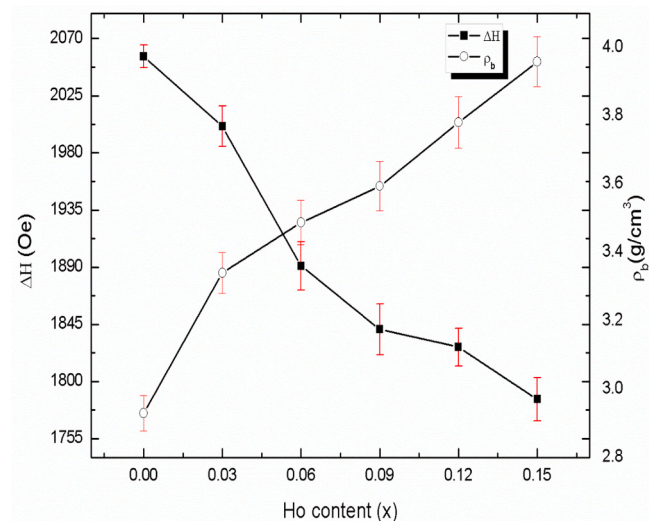


**Fig. 6.** The dependence of bulk density ($\rho_b$) and FMR linewidth ($\Delta H$) on composition.

**Table 2**
All investigated magnetic parameters of $Li_{1.2}Ni_{0.4}Ho_xFe_{2-x}O_4$ (x = 0.00–0.15) nanoferrites.

| Ho content | $H_{res}$ (Oe) | $\Delta H$ (Oe) | $M_s$ (emu/g)[15] | Bulk density $\rho_b$ (g/cm³) |
|---|---|---|---|---|
| 0.00 | 7637 | 2056 | 57.9 | 2.93 |
| 0.03 | 7639 | 2001 | 45.0 | 3.34 |
| 0.06 | 7619 | 1891 | 38.6 | 3.49 |
| 0.09 | 7637 | 1841 | 32.1 | 3.59 |
| 0.12 | 7628 | 1827 | 23.0 | 3.78 |
| 0.15 | 7633 | 1786 | 18.3 | 3.96 |

particles [25]. In polycrystalline magnetic oxides, the contribution to $\Delta H$ primarily arises from two parts; $\Delta H = \Delta H_k + \Delta H_p$, where $\Delta H_k$ is the contribution arising from crystalline anisotropy and $\Delta H_p$ is the line broadening arising from pores. In the case of ferrites, the weak magneto-crystalline anisotropy, which results from the randomly distributed anisotropy axes, rules out the contribution of $\Delta H_k$. At the
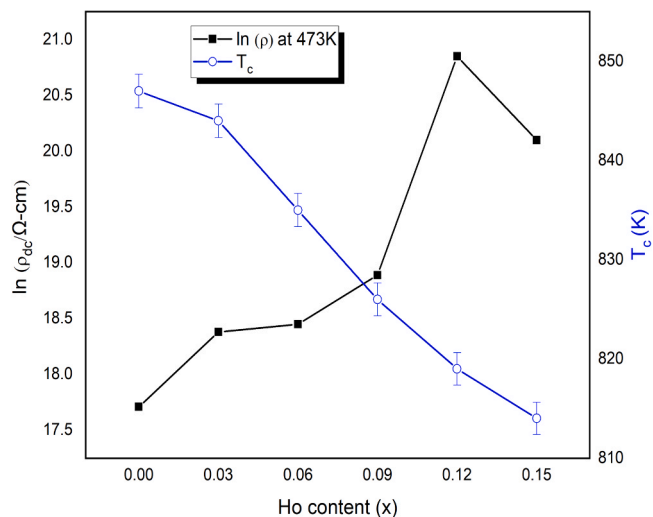


**Fig. 7.** Composition-dependent ln ($\rho_{dc}$) at 473 K and $T_c$ of $Li_{1.2}Ni_{0.4-}Ho_xFe_{2-x}O_4$ ferrites.
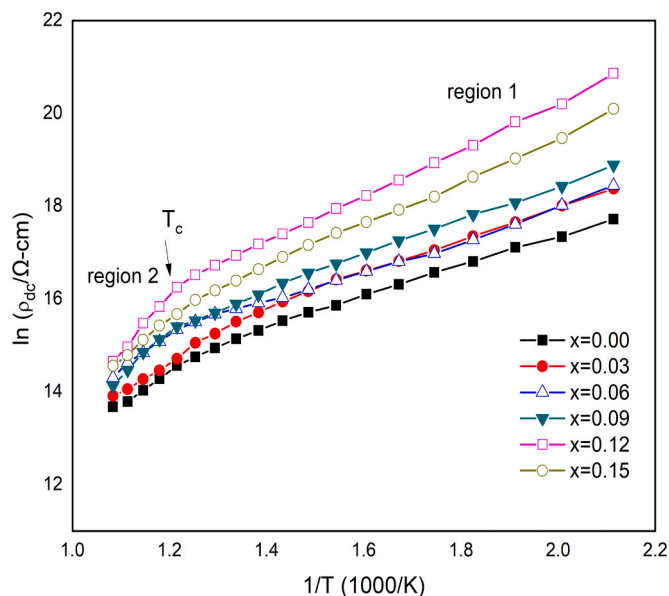


**Fig. 8.** Temperature-dependence of ln ($\rho_{dc}$) of $Li_{1.2}Ni_{0.4}Ho_xFe_{2-x}O_4$ ferrites.

same time, $\Delta H_p$ constitutes a central contribution to $\Delta H$. The resonance field ($H_{res}$) values obtained for all samples vary between $7619 - 7639$ Oe. The $H_{res}$ positions show a non-linear change as a function of Ho concentration. In polycrystalline materials, crystallites and pores have a random distribution that causes the FMR line position to differ from point to point, broadening and shifting the resonance peak. The inset of Fig. 5 is the resonance signal measured from the FMR absorption profile of the undoped sample. The values of all magnetic parameters are presented in Table 2.

### 3.6. DC resistivity measurements

A two-probe current-voltage (IV) technique is employed to study the dc electrical parameters of the Ho-substituted $Li_{1.2}Ni_{0.4}Ho_xFe_{2-x}O_4$ (x = 0–0.15) ferrite pellets across a temperature scale of 473–948 K. The variation of electrical dc resistivity concerning the composition is presented at 473 K in Fig. 7. It can be noticed that the dc resistivity first rises from $4.9 \times 10^7$ to $1.2 \times 10^9$ $\Omega$-cm by increasing the Ho content until x = 0.12 and then decreases after that. Incorporating Ho in place of Fe

**Table 3**
Electrical parameters of $Li_{1.2}Ni_{0.4}Ho_xFe_{2-x}O_4$ nanoferrites with x = 0.00–0.15.

| Ho content | $\rho_{dc}$ (Ω cm) t at 473 K | $T_c$ (K) | $E_p$ (eV) | $E_f$ (eV) | Activation energy difference (eV) | $\mu_d$ (cm²/V.s) at 473 K |
|---|---|---|---|---|---|---|
| | | | | | $\Delta E = E_p - E_f$ | |
| 0.00 | $4.96 \times 10^7$ | 847 | 1.035 | 0.709 | 0.324 | $7.41 \times 10^{-12}$ |
| 0.03 | $9.58 \times 10^7$ | 844 | 1.110 | 0.777 | 0.333 | $3.47 \times 10^{-12}$ |
| 0.06 | $1.03 \times 10^8$ | 835 | 1.170 | 0.834 | 0.335 | $3.19 \times 10^{-12}$ |
| 0.09 | $1.59 \times 10^8$ | 826 | 1.211 | 0.868 | 0.342 | $2.07 \times 10^{-12}$ |
| 0.12 | $1.15 \times 10^9$ | 819 | 1.226 | 0.866 | 0.360 | $2.80 \times 10^{-13}$ |
| 0.15 | $5.36 \times 10^8$ | 814 | 1.227 | 0.875 | 0.351 | $5.92 \times 10^{-13}$ |
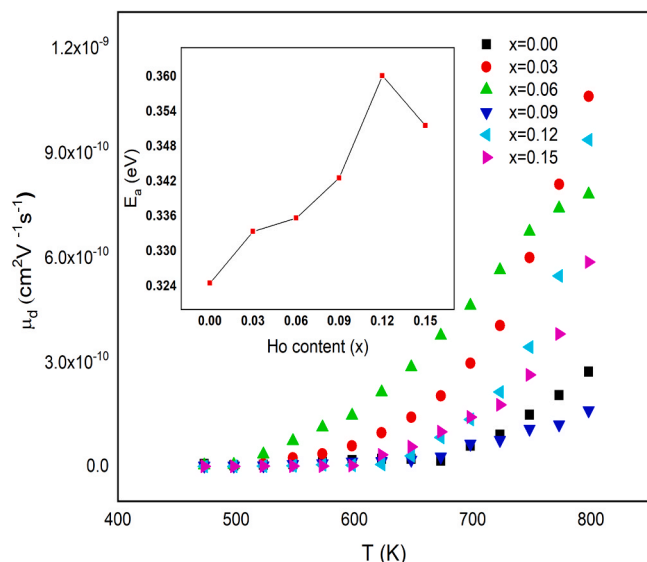


**Fig. 9.** Temperature-dependent drift mobility of $Li_{1.2}Ni_{0.4}Fe_{2-x}H_xO_4$ ferrites. The inset is $E_a$ (ΔE) as a function of Ho-content.

on B sites reduces the hopping frequency of electron transfer between ferrous and ferric states, decreasing the conduction process and consequently increasing the resistivity. Moreover, the particles with small grains have high values of resistivity associated with them and vice versa. The highest value of resistivity ($1.15 \times 10^9$ Ω-cm) is observed for the composition with x = 0.12, which would allow this material to be used in high-frequency applications [26]. It is evident from the near-linear slope of $log\ \rho_{dc}$ versus $1/T$ curves over wide temperature ranges as presented in Fig. 8 that the dc resistivity exhibits a thermally activated behavior, which is consistent with the semiconducting behavior of soft ferrites. This decline in resistivity as a function of temperature could be due to the rise in drift mobility of thermally-activated charge transporters, which become more activated with increasing temperature [27,28]. The activation energies for both ferromagnetic and paramagnetic regions are calculated from the slopes of $log\ \rho$ vs. $1/T$ plots by using the Arrhenius equation ($\rho = \rho_0 e_B^{T \cdot \Delta E/K}$) for all $Ho^{3+}$ concentrations and are presented in Table 3. The values of activation energies in the ferromagnetic region ($E_f$) are found to be smaller than those in the paramagnetic region ($E_p$), which agrees with the theory of Turov and Irkhin [29] and supports the disordering and ordering setting of atoms in ferromagnetic and paramagnetic states, respectively. In the case of the paramagnetic state, more energy is required for charge carriers to transfer than for the ferromagnetic state [30].

It is also observed that the compositions with higher resistivity values have greater activation energies and vice versa. In general, the probability of electron hopping responsible for electrical conduction in

ferrites depends upon the activation energy, which is associated with the electronic energy barrier experienced by the conduction electrons during the hopping process. Thus, a high activation energy involves a high electrical resistivity [31,32]. The difference in activation energies ($\Delta E = E_p-E_f$) for Ho-doped Li-Ni samples varies between 0.32 and 0.36 eV. The $\Delta E$ ($E_a$) versus Ho concentration is shown in the inset of Fig. 9.

The Curie temperature ($T_c$) as a function of Ho concentration is noted to reduce from 847 to 814 K. This decreasing trend of $T_c$ with rising the number of Ho ions can be identified based on available magnetic cations on tetrahedral and octahedral positions as well as the possible magnetic interactions among them [33]. The substitution of $Ho^{3+}$ ions in place of $Fe^{3+}$ ions at octahedral lattice sites leads to a decline in the $Fe_A^{3+}$ - $O^{2-}$ - $Fe_B^{3+}$ type of A-B exchange interactions. As the strength of A-B magnetic interactions states $T_c$, the damping of A-B interactions results in a decline of $T_c$. The drift mobility is evaluated using the relation $\mu_d = 1/ne\rho_{dc}$, where n is the concentration of charge carriers, e is the electron charge, and $\rho_{dc}$ is the dc resistivity. The drift mobility drops from $7.4 \times 10^{-12}$ to $2.8 \times 10^{-13}$ cm²V⁻¹s⁻¹ up to x = 0.12 and then increases again, showing an inverse relation with the resistivity behavior [34]. A linear temperature dependence of $\mu_d$ can be seen from Fig. 9, as the drift mobility of electric charge transporters increases with the increase in temperature. The carrier concentration $n$ is determined from the relation $n = N_A * \rho_b * P_{Fe}/M$, where $\rho_b$, the bulk density of the annealed material, $N_A$, the Avogadro number, $M$ the molecular weight, and $P_{Fe}$ is the total Fe atoms present in the typical composition [35]. The carrier concentration $n$ is observed to increase from $1.70 \times 10^{22}$ to $1.97 \times 10^{22}$ cm⁻³. Since both the bulk density and the molecular weight increased with increasing the Ho concentration, this increase in carrier concentration may be a consequence of the bulk density increasing more strongly with Ho concentration than the molar weight.

## 4. Discussion

The synthesized nanomaterials are observed to be about 50 nm in size as investigated by TEM analysis. By looking at SEM images, it can be seen clearly that the densification is enhanced as a function of Ho addition, which is consistent with the increase in bulk density of these materials. The cation distributions of the Li, Ni, Ho, and Fe cations at their respective lattice sites were calculated via the Bertaut method. A dense microstructure of prepared nanomaterials is required to reduce microwave losses. The Ho substitution in Li-Ni based ferrites leads to a denser crystal structure (bulk density; 2.93–3.96 g/cm³), as reported in our previous study [15], which consequently reduces the FMR losses from 2056 to 1786 Oe and increases the electrical resistivity from $4.96 \times 10^7$ to $5.36 \times 10^8$ Ω-cm. These obtained results are much better than the ones for the Ho-substituted Li-Mn and Li-Co ferrites [33,36] reported in previous studies. Incorporation of Ho in Li-Ni ferrites remarkably reduces the microwave losses (FMR line width) and enhances the resistivity, which makes them the better choice over other doped Li-based ferrites for microwave technologies.

## 5. Conclusion

Ho-substituted Li-Ni nano-ferrites synthesized via the sol-gel method are extensively examined by SEM, XPS, TEM, FMR, and IV analysis. The TEM study exhibited the high crystallinity and narrow-sized spherical distributions of the prepared nanomaterials with a particle size of ∼ 50 nm. Surface morphology revealed a dense, uniform spherical distribution as a function of Ho ions. The XPS analysis confirmed the presence of all constituent elements, such as Li, Ni, Ho, Fe, and O, with different valence states. An FMR study revealed a reduction in FMR line width (2056–1786 Oe) as a function of Ho concentration, which is well-consistent with a drop in porosity. Electrical measurements have shown that samples possess high resistivity and vice versa. The temperature-dependent dc resistivity confirms the prepared ferrites'

semiconducting nature and low mobility. Consequently, a cutdown in microwave losses required a uniform and dense microstructure. The concluded FMR and electrical parameters provide the understanding necessary to design microwave devices.

## CRediT authorship contribution statement

**Alina Manzoor:** Stoichiometric calculations, methodology, draft preparation, experiment. **Aamir Shahzad:** editing, software. **Wolfgang Kuch:** XPS and FMR analysis, co-supervision, reviewing. **Tauqir Shinwari:** Experimental procedure (XPS and FMR experiments). **Ivar Kumberg**: XPS experiment. **Yasser A. Shokr**: FMR experiment. **Muhammad Azhar Khan**: Supervision, writing – reviewing.

## Declaration of Competing Interest

The authors declare that they have no known competing financial interests or personal relationships that could have appeared to influence the work reported in this paper.

## Data Availability

The data are available from the corresponding authors upon reasonable request.

## Acknowledgment

## References

[1] V. Sviatoslav, et al., Loss separation and thermal studies of Fe/SiO$_2$/ferrite soft magnetic composites, J. Alloy. Compd. 945 (2023), 169254.

[2] S. Dobák, et al., Magnetic losses in soft ferrites, Magnetochemistry 8 (2022) 60.

[3] N. Li, et al., Microstructural and ferromagnetic resonance properties of epitaxial nickel ferrite films grown by chemical vapor deposition, Appl. Phys. Lett. 101 (2012), 132409.

[4] N. Mo, Y.-Y. Song, C.E. Patton, High-field microwave effective linewidth in polycrystalline ferrites: physical origins and intrinsic limits, J. Appl. Phys. 97 (2005), 093901.

[5] S.S. Kalarickal, et al., Ferromagnetic resonance linewidth mechanisms in polycrystalline ferrites: Role of grain-to-grain and grain-boundary two-magnon scattering processes, Phys. Rev. B 79 (2009), 094427.

[6] A. Heeger, T. Blocker III, S.K. Ghosh, Slow and fast relaxation in magnetic resonance in ferrimagnetic MnFe$_2$O$_4$, Phys. Rev. 134 (1964) A399.

[7] S. Yamada, E. Otsuki, Analysis of eddy current loss in Mn–Zn ferrites for power supplies, J. Appl. Phys. 81 (1997) 4791–4793.

[8] H. Suhl, Theory of the magnetic damping constant, IEEE Trans. Magn. 34 (1998) 1834–1838.

[9] G. Aravind, M. Raghasudha, D. Ravinder, Electrical transport properties of nano crystalline Li–Ni ferrites, J. Mater. 1 (2015) 348–356.

[10] M.F. Al-Hilli, S. Li, K.S. Kassim, Microstructure, electrical properties and Hall coefficient of europium-doped Li–Ni ferrites, Mater. Sci. Eng.: B 158 (2009) 1–6.

[11] M.A. Islam, M. Zahidur Rahaman, Md .Mehedi Hasan, A.K.M. Akther Hossain, Analysis of grain growth, structural and magnetic properties of Li-Ni-Zn ferrite under the influence of sintering temperature, Heliyon 5 (2019), e01199.

[12] M. Ramesh, G.S.N. Rao, K. Samatha, B.P. Rao, Cation distribution of Ni–Cu substituted Li-ferrites, Ceram. Int. 41 (2015) 1765–1770.

[13] N. Kumar, et al., Physical properties of Pr-substituted Li/Ni ferrite magnetic materials at nanometric scale for its multifunctional applications in industries/ environment and their cytotoxicity, lymphocyte studies as nanomedicine, Appl. Nanosci. 11 (2021) 2847–2859.

[14] S. Aslam, et al., Structural, optical and magnetic elucidation of co-doping of Nd$^{3+}$ and Pr$^{3+}$ on lithium nanoferrite and its technological application, Results Phys. 12 (2019) 1334–1339.

[15] A. Manzoor, et al., Influence of B-site cations ordering on magnetization and dielectric relaxations in Li–Ni spinel ferrites, Ceram. Int. 47 (2021) 22662–22668.

[16] M. Farid, et al., SEM, FTIR and dielectric properties of cobalt substituted spinel ferrites, J. Ovon Res. 11 (2015) 1–10.

[17] W.E. Lee, M. Rainforth, Ceramic Microstructures: Property Control by Processing, Springer Science & Business Media, 1994.

[18] M.N. Akhtar, A.A. Khan, M.N. Akhtar, M. Ahmad, M.A. Khan, Structural Rietveld refinement, morphological and magnetic features of Cu doped CoCe nanocrystalline ferrites for high frequency applications, Phys. B: Condens. Matter 561 (2019) 121–131.

[19] Q.J. Han, D.H. Ji, G.D. Tang, Z.Z. Li, X. Hou, W.H. Qi, S.R. Liu, R.R. Bian, Estimating the cation distributions in the spinel ferrites Cu$_{0.5−x}$Ni$_{0.5}$Zn$_x$Fe$_2$O$_4$ (0.0≤ x≤ 0.5), J. Magn. Magn. Mater. 324 (2012) 1975–1981.

[20] M.N. Akhtar, A.B. Sulong, M.N. Akhtar, M.A. Khan, Systematic Study of Ce$^{3+}$ on the structural and magnetic properties of Cu nanosized ferrites for potential applications, J. Rare Earths 36 (2017) 156–164.

[21] J. Li, H. Yuan, G. Li, Y. Liu, J. Leng, Cation distribution dependence of magnetic properties of sol–gel prepared MnFe$_2$O$_4$ spinel ferrite nanoparticles. J. Magn. Magn. Mater. 322 (2010) 3396–3400.

[22] H. Yue, W. Zhang, B. Yu, Y. Hu, Y. Lu, Y. Chen, D. Yang, Three-dimensional porous cobalt ferrite and carbon nanorod hybrid network as highly efficient electrocatalyst for oxygen evolution reaction, J. Mater. Sci. 55 (2020) 11489–11500.

[23] S.S. Teixeira, et al., Nanostructured LiFe$_5$O$_8$ by a biogenic method for applications from electronics to medicine, Nanomaterials 11 (2021) 193.

[24] M. Osial, P. Rybicka, M. Pękała, G. Cichowicz, M.K. Cyrański, P. Krysiński, Easy synthesis and characterization of holmium-doped SPIONs, Nanomaterials 8 (2018) 430.

[25] G. Thirupathi, R. Singh, Structural and FMR lineshape analysis of Mn Zn-ferrite nanoparticles. AIP Conf. Proc. 1665, 2015, 050133.

[26] T.W. Mammo, et al., Studies of structural, morphological, electrical, and magnetic properties of Mg-substituted Co-ferrite materials synthesized using sol-gel autocombustion method, Phys. B: Condens. Matter 523 (2017) 24–30.

[27] M. Kamran, M. Anis-ur-Rehman, Influence of La$^{3+}$ substitutions on structural, dielectric and electrical properties of spinel cobalt ferrite, Ceram. Int. 49 (2023) 7017–7029.

[28] M.I. Arshad, et al., Structural, optical, electrical, dielectric, molecular vibrational and magnetic properties of La$^{3+}$ doped Mg–Cd–Cu ferrites prepared by Co-precipitation technique, Ceram. Int. 48 (2022) 14246–14260.

[29] E.A. Turov, V.G. Shavrov, Broken symmetry and magnetoacoustic effects in ferro and antiferromagnetics, Sov. Phys. Uspekhi 26 (1983) 593.

[30] V.K. Lakhani, K.B. Modi, Effect of Al$^{3+}$ substitution on the transport properties of copper ferrite, J. Phys. D: Appl. Phys. 44 (2011) 245403.

[31] I.H. Gul, W. Ahmed, A. Maqsood, Electrical and magnetic characterization of nanocrystalline Ni–Zn ferrite synthesis by co-precipitation route. J. Magn. Magn. Mater. 320 (2008) 270–275.

[32] P.V.B. Reddy, B. Ramesh, C.G. Reddy, Electrical conductivity and dielectric properties of zinc substituted lithium ferrites prepared by sol–gel method. Phys. B: Condens. Matter 405 (2010) 1852–1856.

[33] A. Manzoor, M.A. Khan, W. Kuch, Correlation between ferromagnetic resonance and densification of RE substituted polycrystalline ferrites, Ceram. Int. 44 (2018) 13328–13334.

[34] K. Hussain, et al., Study of structural, optical, electrical and magnetic properties of Cu$^{2+}$ doped Zn$_{0.4}$Co$_{0.6−x}$Ce$_{0.1}$Fe$_{1.9}$O$_4$ spinel ferrites, Phys. B: Condens. Matter 584 (2020), 412078.

[35] M.A. Khan, M. ul Islam, M.A. Iqbal, M. Ahmad, M.F. Din, G. Murtaza, I. Ahmad, M. F. Warsi, Magnetic, ferromagnetic resonance and electrical transport study of Ni$_{1-x}$Tb$_x$ Fe$_2$O$_4$ spinel ferrites, Ceram. Int. 40 (2014) 3571–3577.

[36] A. Manzoor, M.A. Khan, T. Alshahrani, M.H. Alhossainy, M. Sharif, T. Munir, M. I. Arshad, M.A. Iqbal, Effect of Ho$^{3+}$ ions on microwave losses and high-temperature electrical behavior of Li-based magnetic oxides, Ceram. Int. 47 (2021) 4633–4642.